Reworking of atmospheric sulfur in a Paleoarchean hydrothermal system at Londozi, Barberton Greenstone Belt, Swaziland

Desiree L. Roerdink [a,b,*], Paul R.D. Mason [b], Martin J. Whitehouse [c], Fraukje M. Brouwer [d]

[a] Centre for Geobiology, Department of Earth Science, University of Bergen, Allégaten 41, N-5007 Bergen, Norway
[b] Department of Earth Sciences, Utrecht University, Budapestlaan 4, 3584 CD Utrecht, The Netherlands
[c] Department of Geosciences, Swedish Museum of Natural History, SE-10405 Stockholm, Sweden
[d] Geology and Geochemistry, VU Amsterdam, De Boelelaan 1085, 1081 HV Amsterdam, The Netherlands

ARTICLE INFO

ABSTRACT

Anomalous fractionation of the minor isotopes of sulfur (Δ^{33}S, Δ^{36}S) in Archean pyrite is thought to reflect photochemical reactions in an anoxic atmosphere, with most samples falling along a reference array with Δ^{36}S/Δ^{33}S $\approx$ −1. Small deviations from this array record microbial sulfate reduction or changes in atmospheric source reactions. Here, we argue that reworking of atmospheric sulfur with distinct minor sulfur isotope ratios (Δ^{36}S/Δ^{33}S $\neq$ −1) produced additional variability in sulfide Δ^{33}S and Δ^{36}S-values in a 3.52 Ga hydrothermal barite deposit at Londozi, Barberton Greenstone Belt, Swaziland. In situ measurement of the four stable sulfur isotopes in pyrite revealed Δ^{36}S–Δ^{33}S relationships and a Δ^{36}S/Δ^{33}S trend (−3.2 ± 0.4), which is significantly different from the co-variation between Δ^{36}S and Δ^{33}S in the co-existing barite that reflects ambient Paleoarchean seawater sulfate. This argues against biological or thermochemical sulfate reduction at the time of barite deposition, and requires incorporation of sulfide generated in a chemically distinct atmosphere before 3.52 Ga. We propose a model that combines reworking of this sulfur by hydrothermal leaching, deep mixing with juvenile sulfur and surface mixing with biogenic sulfide to explain the observed variation in δ^{34}S, Δ^{33}S and Δ^{36}S. These interactions between abiotic and biological processes in the Londozi hydrothermal system complicate the interpretation of biosignatures based on deviations in Δ^{33}S and Δ^{36}S from the Archean reference array.

© 2016 The Authors. Published by Elsevier B.V. This is an open access article under the CC BY-NC-ND license (http://creativecommons.org/licenses/by-nc-nd/4.0/).

1. Introduction

Sulfur cycling in seafloor hydrothermal systems involves high-temperature abiotic sulfate reduction by ferrous iron minerals, leaching of sulfur from volcanic host rocks and direct degassing of magmatic SO_2, as well as microbial sulfate reduction and sulfide oxidation in lower temperature venting areas (Ohmoto and Goldhaber, 1997; Shanks, 2001). The relative importance of these processes can be evaluated from multiple sulfur isotopic compositions (δ^{33}S, δ^{34}S, δ^{36}S) of hydrothermal sulfide and sulfate minerals. Experimental and modeling work has shown that biological transformations, isotope mixing and equilibrium reactions follow slightly different mass-dependent fractionation laws that result in small but measurable variations in Δ^{33}S (δ^{33}S − 1000 × ((1 + δ^{34}S/1000)$^{0.515}$ − 1)) and Δ^{36}S (δ^{36}S − 1000 × ((1 + δ^{34}S/1000)$^{1.91}$ − 1)), and enable identification of sulfur

sources even when ^{34}S/^{32}S ratios (δ^{34}S) are inconclusive (Farquhar et al., 2003; Johnston et al., 2007, 2005; Ono et al., 2006). For example, using this multiple sulfur isotope approach, Ono et al. (2007) showed that leaching of basaltic sulfur dominated over biogenic sources of sulfide at sediment-free mid-ocean ridges.

The same principle can be applied to assess roles of abiotic and biological processes in the formation of sulfide minerals in Archean (3.8–2.5 Ga) hydrothermal environments. However, Archean sulfide sources carry additional variation in Δ^{33}S and Δ^{36}S due to mass-independent fractionation of sulfur isotopes (S-MIF) during SO_2 photolysis in the anoxic early atmosphere (Farquhar et al., 2000; Pavlov and Kasting, 2002). Many sulfide samples older than ca. 2.45 Ga define a negative correlation between the minor isotope signatures, which is described by Δ^{36}S/Δ^{33}S $\approx$ −1 and is assumed to reflect a common photochemical reaction pathway for nearly two billion years (Farquhar et al., 2000; Johnston, 2011; Kaufman et al., 2007; Thomassot et al., 2015). Small deviations from this array corresponding with large mass-dependent sulfur isotope fractionation (δ^{34}S) measured in pyrite have been cited as evidence for early microbial activity in hydrothermally-influenced marine

settings (Roerdink et al., 2013; Shen et al., 2009; Ueno et al., 2008). Alternatively, larger variations in $\Delta^{36}S/\Delta^{33}S$ at specific time intervals in the rock record have been interpreted to reflect temporal changes in atmospheric chemistry (Farquhar et al., 2007), for example due to biogenic methane production (Domagal-Goldman et al., 2008; Zerkle et al., 2012) or changes in volcanic fluxes of reduced and oxidized sulfur species (Halevy et al., 2010). Recent work demonstrated that such shifts may have already occurred in the early Paleoarchean (Wacey et al., 2015).

Assuming that contributions of non-seawater-derived sulfide were equally important in the Archean as in modern seafloor hydrothermal systems, these fluctuations in atmospheric conditions raise the question whether reworking of older atmospheric sulfur from host rocks could have generated additional variability in $\Delta^{33}S$ and $\Delta^{36}S$ in ancient hydrothermal sulfide minerals. Although the preservation of S-MIF signatures implies that biological or magmatic redox cycling of atmospheric sulfur species must have been limited on the early Earth (Halevy et al., 2010), non-zero $\Delta^{33}S$-values were observed in 2.7 Ga komatiite-hosted Fe–Ni sulfide deposits formed by magmatic assimilation of older atmospheric sulfur in volcano-sedimentary rocks (Bekker et al., 2009). In addition, observation of S-MIF in geologically young diamond- and olivine-hosted igneous sulfides suggests that dilution with mantle-derived sulfur does not necessarily erase atmospherically-derived isotope signatures (Cabral et al., 2013; Farquhar et al., 2002). As such, reworking of surface material may have been more important for variations in $\Delta^{33}S$ and $\Delta^{36}S$ in Archean volcanic-hydrothermal deposits than previously considered, possibly complicating the interpretation of ancient biosignatures due to mixing of multiple atmospheric and microbial minor isotopic arrays. Here, we test this hypothesis using *in situ* quadruple sulfur isotope analysis of pyrite from the 3.52 Ga Paleoarchean Londozi barite deposit in the Theespruit Formation of the Barberton Greenstone Belt, Swaziland. Radiogenic isotope data from metavolcanics in the same formation have been interpreted to reflect involvement of older crustal material in the magma source region (Kröner et al., 2013; Kröner et al., 1996; Van Kranendonk et al., 2009), whereas barite sulfur isotopic compositions suggest local microbial reduction of seawater sulfate (Roerdink et al., 2012). These unique features enable us to assess the roles of reworking versus microbial fractionation in determining S-MIF variability in one of the oldest hydrothermal systems preserved in the rock record.

2. Geological background

2.1. Barite deposit

The Londozi barite deposit occurs within a succession of metavolcanics belonging to the *ca.* 3.55–3.51 Ga Theespruit Formation (Kröner et al., 2013, 1996) of the Lower Onverwacht Group, on the eastern flank of the Steynsdorp anticline in the southernmost part of the Barberton Greenstone Belt (S26°11.359′ E31°00.511′, see inset in Fig. 1c). Mining operations in the area demonstrated the presence of a barite-bearing zone that is up to twelve meters thick and can be traced continuously over approximately 1.3 km along strike (Barton, 1982). The barite is finely crystalline and contains microcrystalline pyrite, sphalerite and rare chalcopyrite and galena (Reimer, 1980). The occurrence of the barite within a volcanic sequence and the presence of base metal sulfides has been interpreted to reflect a hydrothermal origin of the deposit (Barton, 1982; Reimer, 1980), which is substantiated by our field and isotopic data. Deformed pillow basalts (Fig. 1a) underlying the barite horizon provide direct evidence for subaqueous volcanic activity and indicate the presence of a magmatic heat source driving fluid convection. In addition, an alteration mineral assemblage with celsian, hyalophane, epidote, witherite and armenite that was found in metabasalts immediately below the barite (Fig. 1b) but not in the overlying felsic volcanic rocks suggests that barite precipitated as a primary deposit, since late-stage replacement reactions or precipitation during burial and metamorphism should alter rocks on both sides of the deposit (cf. Van Kranendonk and Pirajno, 2004). Sulfur isotopic compositions of the Londozi barite deposit have been interpreted to reflect a seawater source of the sulfate (Roerdink et al., 2012), consistent with barite formation as a submarine volcanic-hydrothermal deposit.

2.2. Host rocks

Metavolcanics underlying the barite horizon are of mafic to ultramafic composition and occur as pillowed and foliated massive beds, some of which are strongly silicified. Mineral assemblages consist of hornblende, plagioclase, quartz, biotite, ilmenite and garnet and are characteristic for the amphibolite facies metamorphism in the Steynsdorp region that reached temperatures of 640–660 °C at a pressure of 10–13 kbar (Lana et al., 2010). The barite deposit is overlain by strongly foliated mica schists with quartz, K-feldspar, plagioclase and biotite, that have been interpreted to reflect sheared felsic tuffs (Reimer, 1980). The contact between these felsic rocks and the barite is sharp, in contrast to the gradual transition from the metabasalts into altered metabasalts in which small-scale barite infiltrations occur below the main barite horizon. Lens- and sigmoidal-shaped fragments of metabasaltic host rocks and chert are also found within the barite, but intense deformation complicates the interpretation of original petrographic relations.

2.3. Age of the barite deposit

SIMS dating of zircon from felsic schists and metavolcanics in the lowermost part of the Theespruit Formation in the Londozi area yielded ages of 3552 ± 1 Ma (6 grains) and 3530 ± 4 Ma (12 grains), respectively (Kröner et al., 2013 and pers. comm.), suggesting an early Paleoarchean age for the deposit. To obtain a more specific age for the barite, we performed LA-ICP-MS analyses on prismatic and oscillatory zoned zircon grains from the felsic schists immediately overlying the main barite horizon at 0.5–1.0 m from the contact (see Supplementary Information for details of the sample preparation and analytical method). A total of 27 grains were analyzed, with 24 grains yielding ages at 95–105% concordance (Supporting Dataset S1). The age of the felsic tuffaceous schist was determined using the ISOPLOT TuffZirc algorithm (Ludwig, 2008), giving a $^{207}Pb/^{206}Pb$ deposition age of 3522 +13/−8 Ma based on 20 concordant grains (Fig. 1c), compared to a concordia age of 3531 ± 19 Ma ($n = 27$, MSWD = 1.7). Interpretation of this result as the age of crystallization is consistent with Th/U ratios ranging from 0.42 to 0.72 (Hoskin and Schaltegger, 2003; Rubatto, 2002; Williams et al., 1996), as well as the oscillatory and lengthwise zoning in euhedral crystals (Supplementary Fig. S1) that is typical for zircon of magmatic origin (Corfu et al., 2003). Therefore, in this paper we adopt an age of 3.52 Ga as the minimum depositional age of the Londozi barite deposit.

3. Material and methods

3.1. Samples

Pyrite-bearing rock fragments were sampled from barite and immediate host rocks collected from surface outcrops of the Londozi deposit. Rock sample TR-03 consists of silicified barite, and the studied fragment of this sample contains 50–500 µm large
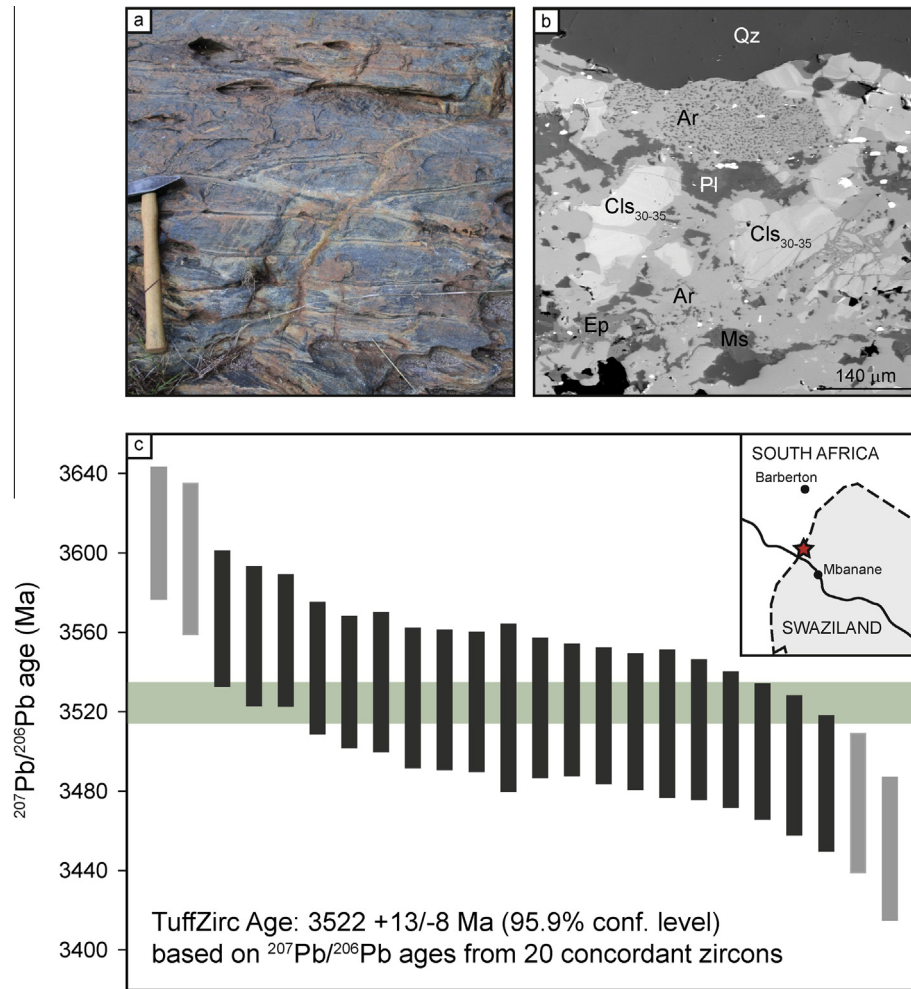
Fig. 1. Figures highlighting the geological background of the Londozi barite deposit. (a) Photo of deformed pillow basalts underlying the barite horizon, indicative of subaqueous volcanic activity. Hammer (*ca.* 30 cm) for scale. (b) Backscattered electron map of the Ba-rich mineral assemblage found in metabasalts below the barite horizon, interpreted to reflect hydrothermal alteration. Qz: quartz, Ar: armenite ($BaCa_2Al_6Si_9O_{30}·2H_2O$), Pl: plagioclase, Cls: celsian-hyalophane ($(K,Ba)Al(Si,Al)Si_2O_8$), Ep: epidote, Ms: muscovite. (c) Results of LA-ICP-MS U–Pb dating of 24 concordant zircon grains from a felsic schist immediately overlying the barite horizon, with four grains being statistically older or younger (shown in light grey). Vertical bars represent individual ages with 2σ errors and horizontal green bar represents the calculated age with 95.9% confidence level. The concordia age for the same dataset was calculated as 3531 ± 19 Ma ($n = 27$, MSWD = 1.7). Inset shows the location of the Londozi barite deposit. (For interpretation of the references to colour in this figure legend, the reader is referred to the web version of this article.)

anhedral to subhedral pyrite grains in barite and chert matrix (Supplementary Fig. S2a). Sample TR-01 is predominantly composed of silicified metabasalt and analyzed rock fragments contain disseminated anhedral pyrite grains of 50–500 μm in a silicate matric with feldspar and hornblende (Supplementary Fig. S2b, S2c). Samples LON-10-21a and LON-10-21b represent different rocks collected from the same location, and consist of both barite and silicified altered metabasalt. Garnet and epidote single crystals (1–3 cm size) were visible in the hand specimen of sample LON-10-21b. The studied rock fragments of sample LON-10-21a contain disseminated anhedral to subhedral pyrite grains of 50–500 μm size that are hosted by a barite and metabasalt matrix with feldspar, hornblende and garnet (Supplementary Fig. S2d, S2e). Analyzed fragments of LON-10-21b contain large anhedral pyrite of 200–5000 μm in barite and metabasalt matrix (mt_A02), 100–1500 μm anhedral pyrite in a metabasalt matrix (mt_A03), and anhedral to subhedral pyrite of 100–1000 μm in a barite and metabasalt matrix (mt_A06) as shown in Supplementary Fig. S2f, S2g, and S2h, respectively. In addition, pyrite from a barite flange (11-ROV-09) collected at the Jan Mayen hydrothermal vent field on the Arctic Mid-Ocean Ridge (Pedersen et al., 2010) was measured

during the session in 2014, as an additional monitor for analytical variations in $\Delta^{33}S$ and $\Delta^{36}S$ in a non-Archean hydrothermal sulfide.

3.2. SIMS sulfur isotope analyses

Rock fragments were mounted in 25 mm diameter polished epoxy mounts that were gold coated for *in situ* sulfur isotope analysis using a CAMECA IMS-1280 ion microprobe at the Swedish Museum of Natural History (Nordsim facility). A sector was cut from the sample blocks to allow co-mounting with epoxy-embedded pyrite standards. Measurements followed the analytical protocol of Whitehouse (2013) with a 10 kV and *ca.* 2 nA Cs$^+$ focused primary beam yielding an average spot size of 10 μm. A 90 s pre-sputter over a 20×20 μm rastered area was used to remove gold coating from the target area, during which detector backgrounds were measured for 30 s. Charge build-up on the sample was prevented using a low-energy electron gun and the magnetic field was locked for each session using NMR regulation. Faraday amplifiers were used for the detection of ^{32}S, ^{33}S and ^{34}S, whereas the low natural abundance of ^{36}S required operation of

an electron multiplier, with additional correction for gain drift on $^{36}S/^{32}S$ during the course of an analytical session based on the regularly interspersed standard analyses.

Samples were measured in four analytical sessions between 2009 and 2014 (for spot locations, see Supplementary Fig. S2a–h). Instrumental mass fractionation was determined by bracketing analyses of unknowns with measurements of Ruttan pyrite, using a $\delta^{34}S$-value of 1.2 ± 0.1‰ for the 2009–2012 sessions (Crowe and Vaughan, 1996) and 1.408 ± 0.006‰ in 2014 (Cabral et al., 2013). Additional analyses of the Balmat pyrite with $\delta^{34}S = 16.12 \pm 1.42$ (Cabral et al., 2013) were used to define the slope of the mass dependent fractionation line, assuming non-MIF $\Delta^{33}S$ and $\Delta^{36}S$ for both reference sulfides (Whitehouse, 2013). An anomalously fractionated reference pyrite from the Isua greenstone belt (sample GGU 278474) was included in each analytical session to monitor the accuracy of mass-independent signatures. Sulfur isotope data were calculated as $\delta^{34}S = [((^{34}S/^{32}S)_{sample}/(^{34}S/^{32}S)_{V\text{-}CDT}) - 1] \times 1000$; $\Delta^{33}S = \delta^{33}S - 1000 \times [(1 + \delta^{34}S/1000)^{0.515} - 1]$ and $\Delta^{36}S = \delta^{36}S - 1000 \times [(1 + \delta^{34}S/1000)^{1.91} - 1]$.

3.3. SIMS data quality assessment

Data for all analytical sessions are reported in Supporting Dataset S2. The average internal precision (1σ) for $\delta^{34}S$ was 0.30‰ in 2009 ($n = 24$), 0.14‰ in 2010 ($n = 31$), 0.23‰ in 2012 ($n = 103$) and 0.08‰ in 2014 ($n = 143$), based on repeated analyses of the Ruttan and Balmat standards and Isua reference pyrite. For $\Delta^{33}S$, internal precision was 0.16‰ in 2009, 0.13‰ in 2010, 0.14‰ in 2012 and 0.06‰ in 2014, and for $\Delta^{36}S$ the internal precision averaged 0.48‰ in 2012 and 0.20‰ during the analytical session in 2014. The accuracy and external precision of mass-independent isotope signatures were monitored using the Isua pyrite 278474, for which previous conventional and SIMS sulfur isotope analyses yielded values of $\delta^{34}S = 2.34 \pm 0.86$‰, $\Delta^{33}S = 3.18 \pm 0.05$‰ and $\Delta^{36}S = -2.20 \pm 0.21$‰ (Baublys et al., 2004; Cabral et al., 2013; Roerdink et al., 2013; Whitehouse, 2013). Our measured values were $\delta^{34}S = 2.51 \pm 0.12$‰ and $\Delta^{33}S = 3.23 \pm 0.17$‰ for the session

in 2009 ($n = 6$, mean $\pm 2\sigma$), $\delta^{34}S = 2.41 \pm 0.06$‰ and $\Delta^{33}S = 3.12 \pm 0.06$‰ for the session in 2010 ($n = 5$), $\delta^{34}S = 2.46 \pm 0.09$‰, $\Delta^{33}S = 3.18 \pm 0.05$‰ and $\Delta^{36}S = -2.1 \pm 0.2$‰ for the session in 2012 ($n = 20$), and $\delta^{34}S = 2.48 \pm 0.06$‰, $\Delta^{33}S = 3.15 \pm 0.02$‰ and $\Delta^{36}S = -2.0 \pm 0.1$‰ for the session in 2014 ($n = 22$). These results indicate an excellent accuracy and long term reproducibility of major and minor sulfur isotope ratios, as well as a precision that is comparable to previous SIMS studies on samples exhibiting S-MIF (Farquhar et al., 2013; Roerdink et al., 2013; Wacey et al., 2015; Whitehouse, 2013). No correlation was found between the standard-normalized secondary ion count rate and $\delta^{33}S$, $\delta^{34}S$ or $\delta^{36}S$ (Supplementary Fig. S3), suggesting that data have not been affected by variable instrumental mass bias. Unlike pyrite analyzed by Wacey et al. (2015) that showed very low count rates relative to their standards (5–10%), our unknown count rates are within 70–130% of the Ruttan standards and results are therefore considerably less susceptible to inaccuracies in the assignment of electron multiplier dead time corrections that could affect ^{36}S. Furthermore, the dead time was electronically gated at 60 ns, which is several times longer than the actual pulse width and precise to ~1 ns. Accurate measurement of $\Delta^{36}S$ is further confirmed by the average $\Delta^{36}S$-value of 0.08 ± 0.10‰ that was measured in modern pyrite from the Jan Mayen hydrothermal vent field (Pedersen et al., 2010), which is expected to display no mass-independent isotope fractionation considering its age.

4. Results

Measured pyrite $\delta^{34}S$-values ($n = 272$) range from -9.14 to 6.62‰ (Fig. 2a) and represent isotope fractionation relative to the Londozi barite of up to ~15‰ (Fig. 2a). Sample TR-03 shows the strongest ^{34}S-depletion with an average $\delta^{34}S$-value of -6.32 ± 0.60‰ ($n = 32$), compared to an average $\delta^{34}S$ of -2.45 ± 0.68‰ for LON-10-21a ($n = 29$), -1.72 ± 0.24‰ for LON-10-21b ($n = 109$) and -0.12 ± 0.22‰ for sample TR-01 ($n = 102$). The $\delta^{34}S$-data show a weakly positive correlation with $\Delta^{33}S$, varying from strongly negative $\Delta^{33}S$-values between -1.77 and -0.65‰ in the most ^{34}S-depleted pyrite in sample TR-03 ($\Delta^{33}S_{avg} = -0.93 \pm 0.05$‰),

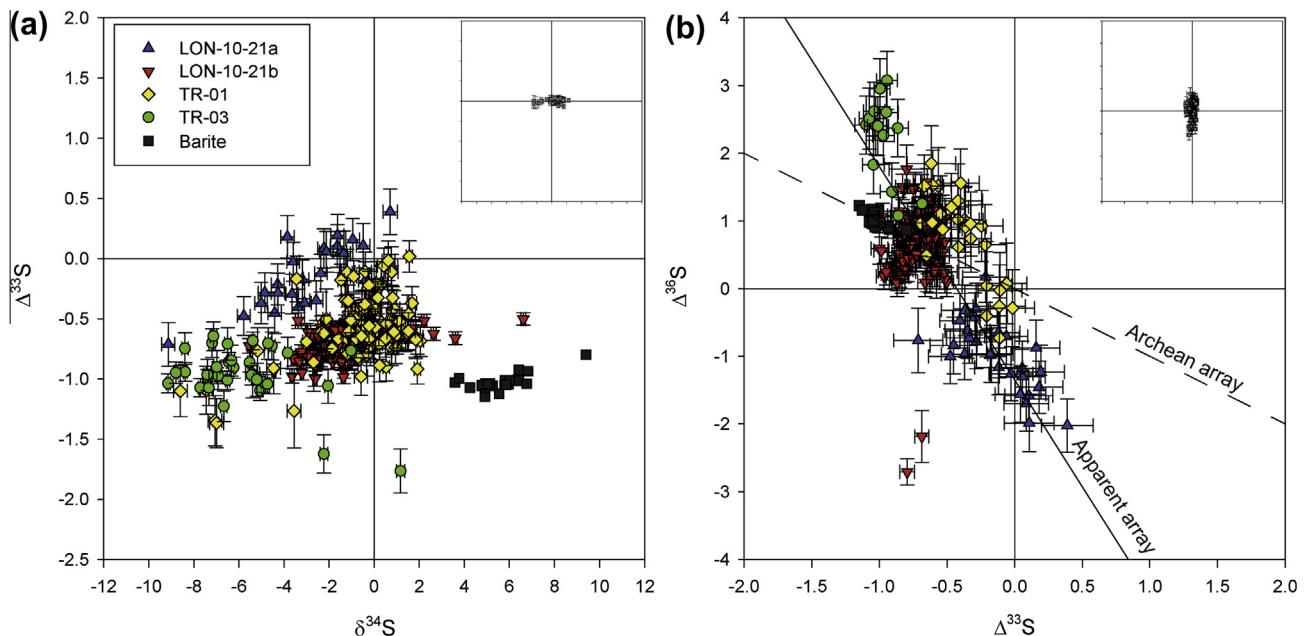**Fig. 2.** Sulfur isotopic compositions of pyrite measured by SIMS. (a) Plot of $\Delta^{33}S$ versus $\delta^{34}S$. (b) Plot of $\Delta^{36}S$ versus $\Delta^{33}S$ with the dashed line representing the Archean reference array ($\Delta^{36}S/\Delta^{33}S = -1$). The apparent array represents the trend line through the pyrite data ($\Delta^{36}S/\Delta^{33}S = -3.2 \pm 0.4$), and not a photolytic array. In both plots, the dark grey squares represent bulk analyses (SF_6 GS-IRMS) of the Londozi barite from Roerdink et al. (2012). Insets show the range in isotopic compositions measured in modern hydrothermal pyrite from the barite-rich Jan Mayen vent field (axes use the same scale as main plots). All error bars are 1σ.

to near-zero values in less fractionated pyrite in samples LON-10-21a ($\Delta^{33}S_{avg} = -0.16 \pm 0.09‰$) and TR-01 ($\Delta^{33}S_{avg} = -0.55 \pm 0.04‰$). The measured range in $\Delta^{33}S$ is consistent with $\Delta^{33}S$-values measured in the Londozi barite on sulfate extracted by Thode reduction and analyzed as SF_6 by gas-source mass spectrometry (Roerdink et al., 2012), and the weak co-variation between $\delta^{34}S$ and $\Delta^{33}S$ is similar to trends observed in South African barite from the 3.26–3.23 Ga Mapepe Formation (Philippot et al., 2012; Roerdink et al., 2013). In contrast, the within-sample $\Delta^{36}S$ variability as well as the variation in $\Delta^{36}S$ between samples is significantly larger than values measured in the barite. Sample LON-10-21b shows the largest range in $\Delta^{36}S$ from -2.7 to $1.8‰$, significantly in excess of analytical precision, and the overall variation in $\Delta^{36}S$ ranges from -2.7 to $3.1‰$ compared to 0.86–$1.23‰$ for the barite (Roerdink et al., 2012). Sample TR-03 shows the most positive $\Delta^{36}S$-values from 1.1 to $3.1‰$, compared to -0.7 to $1.9‰$ for sample TR-01 and -2.0 to $0.3‰$ for sample LON-10-21a. All samples together define a co-variation between $\Delta^{36}S$ and $\Delta^{33}S$ (Fig. 2b) that is described by a slope of -3.2 ± 0.4 and an intercept of -1.4 ± 0.3 ($n = 179$). This is a significant deviation from the Archean reference array ($\Delta^{36}S/\Delta^{33}S \approx -1.0$) (Farquhar et al., 2000), as well as the slope of -0.8 ± 0.5 defined by the minor sulfur isotopic compositions of the Londozi barite (Roerdink et al., 2012). Contrary to the Londozi pyrite, *in situ* sulfur isotope analyses of microscopic pyrite from the modern barite-rich hydrothermal flange of the Jan Mayen vent field demonstrated no significant anomalous isotope fractionation, with $\Delta^{33}S_{avg} = 0.0 \pm 0.1‰$ and $\Delta^{36}S_{avg} = 0.1 \pm 0.1‰$ (see inset on Fig. 2a and b).

5. Discussion

5.1. Non-biogenic origin for variation in $\Delta^{33}S$ and $\Delta^{36}S$

Preservation of significant isotopic heterogeneity within large pyrite grains (Fig. S2a–h and Supplementary Dataset S2), within individual samples and between samples (Fig. 2) suggests that sulfur isotope ratios were not homogenized or re-equilibrated with barite during the amphibolite facies metamorphism that affected the Londozi region at 3.23 Ga (Lana et al., 2010), and still reflect fractionation pathways in the ancient hydrothermal system. Although the magnitude of fractionation in $\delta^{34}S$ relative to the barite (*ca.* 15‰) is consistent with microbial sulfate reduction and the variation in $\Delta^{33}S$ could be explained by mixing of this seawater-derived sulfide with juvenile sulfur ($\Delta^{33}S = 0‰$) or minor isotope effects along the metabolic pathway, the broad range of $\Delta^{36}S$-values argues against a purely biological origin for the pyrite. Laboratory culture experiments and models predict small changes in minor isotope ratios during microbial sulfate reduction, but effects for $\Delta^{36}S$ are on the order of 1–2‰ and towards more negative values compared to reactant sulfate (Farquhar et al., 2003; Johnston et al., 2007, 2005). Differences of ~3‰ between the barite and pyrite grains with the most negative $\Delta^{36}S$-values, as well as pyrite that is more ^{36}S-enriched than the barite (Fig. 2b) are thus inconsistent with microbial sulfate reduction. Similarly, minor isotope effects are small for microbial sulfur disproportionation (Johnston et al., 2007) and cannot explain the measured variation in $\Delta^{36}S$. Rayleigh distillation processes in a closed system can produce larger shifts in $\Delta^{36}S$ (Ono et al., 2006), but the observed magnitude of ^{36}S-depletion requires larger fractionations in $\delta^{34}S$ than found in this study. Anomalous fractionation of ^{33}S and ^{36}S was also reported from thermochemical sulfate reduction experiments (Watanabe et al., 2009), but the lack of any significant minor isotope variations in microscopic pyrite from the active high-temperature Jan Mayen vent field (see inset in Fig. 2 and Supporting Dataset S2) suggests that such reactions are not relevant for barite-rich hydrothermal systems. In fact, subsequent

experimental work demonstrated that mass-independent sulfur isotope fractionation in these non-gas phase reactions results from magnetic isotope effects that only produce large variations in $\Delta^{33}S$, without significantly affecting ^{36}S (Kopf and Ono, 2012; Oduro et al., 2011).

Since no known biological or chemical mass-dependent process is consistent with the observed variation in $\Delta^{36}S$, we deduce an atmospheric origin for the large variation in $\Delta^{33}S$ and $\Delta^{36}S$ in the Londozi pyrite. Photolysis and photoexcitation of volcanic SO_2 gas in an anoxic atmosphere generates significant mass-independent fractionation of minor sulfur isotopes, resulting in large values of $\Delta^{33}S$ and $\Delta^{36}S$ (Danielache et al., 2012; Farquhar et al., 2000, 2001; Whitehill and Ono, 2012; Whitehill et al., 2013). In addition, ratios of $\Delta^{36}S/\Delta^{33}S$ in product sulfur species were shown to be dependent on atmospheric chemistry and the wavelength of UV-radiation interacting with the SO_2 gas (Farquhar et al., 2001; Kurzweil et al., 2013; Zerkle et al., 2012). As such, the strongly positive and negative $\Delta^{36}S$-values of the Londozi pyrite (Fig. 2b) could be explained by sulfur produced in an atmosphere that was chemically distinct from the one reflected by the barite. Most importantly, the mismatch with the barite $\Delta^{36}S$–$\Delta^{33}S$ suggests that this modified atmosphere could not have been present at the time the barite was deposited, because that shows the same $\Delta^{36}S/\Delta^{33}S$ as the Archean reference array and is considered to reflect ambient Paleoarchean seawater (Roerdink et al., 2012). Any short-term changes in atmospheric chemistry are likely buffered by this seawater sulfate pool, as suggested by similar $\Delta^{33}S$ and $\Delta^{36}S$-values in similar-aged barite deposits from South Africa and Western Australia (Bao et al., 2007; Roerdink et al., 2012). Alternatively, brief variations in atmospheric chemistry could have produced elemental sulfur with distinct $\Delta^{36}S/\Delta^{33}S$ that was transferred to pyrite via microbial (Philippot et al., 2007) or abiotic (Farquhar et al., 2013; Wacey et al., 2015) pathways. However, predominantly negative $\Delta^{33}S$-values in the pyrite argue against a significant input of elemental sulfur in this system, similar to the dominance of sulfate-derived pyrite observed in other Paleoarchean barite deposits (Ueno et al., 2008; Shen et al., 2009; Roerdink et al., 2013). Introduction of sulfide after deposition of the barite, for example in the Mesoarchean as suggested for layered pyrite in the Barite Valley deposit (Roerdink et al., 2013), seems unlikely as the pyrite occurs as finely disseminated grains in both the barite and the metavolcanics. In addition, most Neoarchean and Mesoarchean sulfide is characterized by $\Delta^{36}S/\Delta^{33}S$ between -1.5 and -0.9 (Kurzweil et al., 2013), which is not steep enough to explain our most ^{36}S-enriched and ^{36}S-depleted sulfur.

Although we explain the large variation in the Londozi pyrite $\Delta^{36}S$ by photochemical reactions in a chemically distinct atmosphere, we do not argue that the $\Delta^{36}S/\Delta^{33}S$ trend represents a photolytic array. In particular, the co-variation defined by all pyrite samples has a distinct non-zero intercept (-1.4 ± 0.3), which conflicts with the requirement of such an array to intersect with the composition of the bulk silicate Earth with $\Delta^{33}S = \Delta^{36}S = 0‰$. As outlined above (Section 3.3), the significantly negative intercept value cannot be explained by analytical issues as all standards and reference samples yield $\Delta^{36}S$ and $\Delta^{33}S$-values consistent with their published values and/or post-Archean age. This leads us to suggest that the initial photolytic array was modified by mixing processes with sulfur with an isotopic composition similar to the barite, producing distinct sulfide pools that are shifted away from the initial photolytic $\Delta^{33}S$ and $\Delta^{36}S$-values to an extent that is dependent on mixing relations. Below, we present a mixing model that is consistent with the geological setting of the Londozi hydrothermal barite deposit.

5.2. Reworking of pre-3.52 Ga atmospheric sulfur

We propose that the mass-independent signatures in the sulfide minerals originated from photochemical reactions in a pre-3.52 Ga

atmosphere and were recycled in the hydrothermal system. Since pyrite δ^{34}S-values provide evidence for additional mass-dependent fractionation, we suggest that the recycled sulfide mixed with reduced sulfate in the seafloor environment. To test our hypothesis, we constructed a three-step mixing model with (1) atmospheric photolysis generating large Δ^{33}S and Δ^{36}S and deposition of produced sulfur species in distinct exit channels, (2) reworking of this material and two-component mixing with juvenile sulfur (δ^{34}S = Δ^{33}S = Δ^{36}S = 0‰) in a magmatic-hydrothermal system, and (3) combination of this non-biogenic sulfide with sulfide derived from microbial reduction of the sulfate reservoir, as represented by the isotopic composition of the barite, on or just below the ocean floor (Fig. 3).

5.2.1. Step 1: Production of atmospheric S-MIF

Constraining the pre-3.52 Ga photochemical array is difficult because of the lack of Δ^{36}S-data from Eoarchean sulfides and discrepancies between photolysis models, experiments and the rock record. Nevertheless, broadband radiation (190–220 nm) photolysis studies are probably most relevant for the Archean atmosphere (Claire et al., 2014), and experimental work by Ono et al. (2013) revealed similarly negative Δ^{36}S/Δ^{33}S-values (−4.6 ± 1.3) to those

observed in our dataset. Although our measured trend (apparent array in Fig. 2) will differ slightly from the slope of the pre-3.52 Ga photolytic array due to the proposed mixing processes, we use the observed Δ^{36}S–Δ^{33}S correlation (Δ^{36}S/Δ^{33}S = −3.2) as a first approximation for the steep photochemical array in our model. This assumption is substantiated by the fact that a line between our data point with the most positive Δ^{36}S-value (i.e. Δ^{33}S = −0.94‰, Δ^{36}S = 3.1‰), presumably reflecting sulfide that is least affected by post-photolysis mixing processes, and the origin of the Δ^{36}S–Δ^{33}S plot (juvenile sulfur) has the same slope of −3.2. We combine this with the average Δ^{33}S/δ^{34}S = 0.10 found by Ono et al. (2013) and others (Lyons, 2007, 2009; Whitehill and Ono, 2012), and assume δ^{34}S = 100‰ for the elemental sulfur and −100‰ for sulfate based on the range of δ^{34}S-values reported from the same experimental work. In addition, we tested an asymmetrical model with stronger S-MIF in the reduced sulfur pool (δ^{34}S = 200‰), as well as a scenario with photolysis producing sulfur isotope ratios according to the Archean reference array with Δ^{36}S/Δ^{33}S = −1.0 (Farquhar et al., 2000) and Δ^{33}S/δ^{34}S = 0.90 (Ono et al., 2003). Our model requires that the oxidized and reduced sulfur were deposited in two different exit channels and incorporated into the rock record as two different reservoirs, for
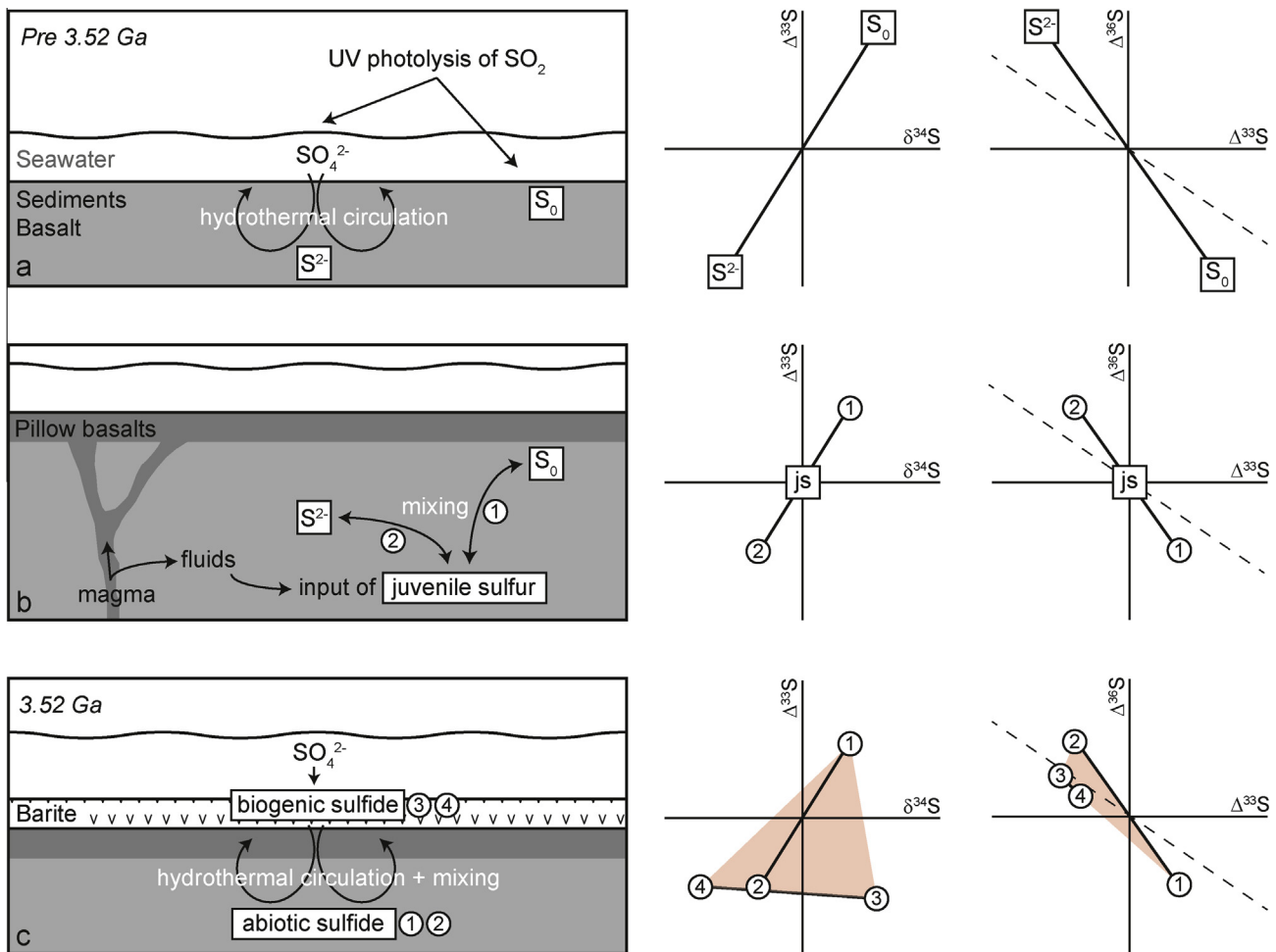

Fig. 3. Cartoons illustrating the hydrothermal reworking model proposed in this study, with inferred changes in Δ^{33}S–δ^{34}S and Δ^{36}S–Δ^{33}S space on the right. (a) Step 1: UV photolysis of SO_2 in a chemically distinct atmosphere before 3.52 Ga generating a steeper trend in Δ^{36}S/Δ^{33}S than the Archean array (dashed line). Elemental sulfur is stored in the rock record whereas atmospheric sulfate is quantitatively reduced to sulfide in hydrothermal systems driven by the heat source related to the subaqueous volcanism. (b) Step 2: mixing of these atmospheric sulfur pools with juvenile sulfur (js) during volcanic-hydrothermal activity, muting the magnitudes of δ^{34}S, Δ^{33}S and Δ^{36}S (i.e. shifted towards zero) and producing Reservoir 1 and Reservoir 2. (c) Step 3: mixing of this deep sulfur with sulfide derived from microbial reduction of seawater sulfate at 3.52 Ga during barite deposition (Reservoirs 3 and 4), creating 4-component mixing fields indicated in red. The isotopic composition of resulting pyrite can be anywhere in this field but should be consistent in both Δ^{33}S–δ^{34}S and Δ^{36}S–Δ^{33}S space. The isotopic composition of the seawater sulfate pool is assumed in this model to be reflected by the barite (cf. Roerdink et al., 2012). (For interpretation of the references to colour in this figure legend, the reader is referred to the web version of this article.)

example as elemental sulfur and sulfide derived from quantitative hydrothermal reduction of seawater sulfate (Fig. 3a), to avoid homogenization and elimination of atmospheric S-MIF signatures. These conditions are consistent with the low levels of oxygen in the Archean atmosphere (Pavlov and Kasting, 2002) and the lack of significant fractionation in $\delta^{34}S$ in Eoarchean sulfides (Mojzsis et al., 2003; Papineau and Mojzsis, 2006; Whitehouse et al., 2005) that suggests limited microbial cycling.

5.2.2. Step 2: Deep mixing of atmospheric and juvenile sulfur

Small-scale isotopic variations were not observed within the individual pyrite grains analyzed in this study, suggesting that the required mixing occurred in a liquid by leaching of sulfur from the host rocks by hot hydrothermal fluids. Such interactions between atmospheric sulfur reservoirs stored in crustal sedimentary rocks (large S-MIF) and juvenile sulfide of magmatic origin (no S-MIF) reduces the magnitude of $\Delta^{33}S$ and $\Delta^{36}S$ but preserves photolytic $\Delta^{36}S/\Delta^{33}S$, as no anomalous isotope effects occur during high-temperature water-rock reactions (Ono et al., 2007). In addition, observation of a different $\Delta^{36}S/\Delta^{33}S$ array in the pyrite and barite suggests that contributions of ambient seawater sulfate to the sulfide pool were small in the Londozi hydrothermal system, implying limited isotopic exchange between dissolved sulfate and sulfide. Therefore, we use the two-component mixing model of Ono et al. (2007) to calculate the end members ($\delta^{34}S_{mix}$) of this abiotic mixing array between juvenile sulfur ($\delta^{34}S_{juv}$) and atmospherically-derived sulfur ($\delta^{34}S_{atm}$):

$$\delta^{34}S_{mix} = a\delta^{34}S_{juv} + (1 - a)\delta^{34}S_{atm} \qquad (1)$$

where a represents the fraction of juvenile sulfur in the mixture. Since $\delta^{34}S_{juv} = \delta^{33}S_{juv} = \delta^{36}S_{juv} = 0‰$, Eq. (1) simplifies to:

$$\delta^{34}S_{mix} = (1 - a)\delta^{34}S_{atm} \qquad (2)$$

Eq. (2) is used to calculate the composition of the mixture between juvenile and photochemical elemental sulfur (Reservoir 1 in Fig. 3b), as well as the pool reflecting juvenile sulfur mixing with sulfide derived from atmospheric oxidized sulfur (Reservoir 2 in Fig. 3b). The same equations were used to calculate values of $\delta^{33}S$ and $\delta^{36}S$, from which $\Delta^{33}S$ and $\Delta^{36}S$ were calculated to take into account that mixing in $\Delta^{36}S$-$\Delta^{33}S$ is not linear.

5.2.3. Step 3: Seafloor mixing of biogenic and abiotic sulfide

In order to explain the observed range in pyrite $\delta^{34}S$-values we argue that the deep hydrothermal fluids, representing mixtures of juvenile and atmospheric sulfur, mixed again on the seafloor with sulfide derived from microbial reduction of a local seawater sulfate reservoir (represented by the barite), generating ^{34}S-depleted sulfide and progressively ^{34}S-enriched residual sulfate that is preserved in the barite (Roerdink et al., 2012). Because of closed-system effects, this biogenic sulfide is represented by two end members: sulfide that is isotopically similar to the barite ($\delta^{34}S = 3‰$, $\Delta^{33}S = -1.10‰$ and $\Delta^{36}S = 1.10‰$) and sulfide that represents the maximum biological isotope effect relative to the barite ($\delta^{34}S = -12‰$, $\Delta^{33}S = -1.02‰$, $\Delta^{36}S = 0.48‰$), indicated as Reservoir 3 and 4 in Fig. 3c, respectively. Values were calculated assuming $^{33}\lambda = 0.510$ and $^{36}\lambda = 1.94$ (Johnston et al., 2007) and $^{34}\alpha = 0.985$, consistent with the magnitude of isotope effects observed in our data. Similar to modern hydrothermal systems where pyrite precipitates upon cooling of the fluid (Reed and Palandri, 2006), pyrite at Londozi would have precipitated from the fluid mixtures when they were expelled on the seafloor at the time of barite-deposition. Because the isotopic composition of the hydrothermal fluid is assumed to have varied with the type of sulfur in its source region (i.e. elemental sulfur versus sulfate-derived sulfide), the resulting pyrite minerals reflect a combination

of the deep and seafloor mixing processes and their sulfur isotope ratios are represented by fields in $\delta^{34}S$-$\Delta^{33}S$ and $\Delta^{36}S$-$\Delta^{33}S$ space (Fig. 3c).

In contrast to the pre-3.52 Ga system where atmospherically-derived elemental sulfur was incorporated in the rock record, there is no isotopic evidence for uptake of 3.52 Ga elemental sulfur in pyrite at the time of barite deposition. A similar absence of elemental sulfur-derived pyrite in barite-rich rocks was observed at the 3.26–3.23 Barite Valley barite deposit, South Africa, which was suggested to be linked to unfavorable environmental conditions (high SO_4^{2-} and low Fe^{2+}) for elemental sulfur disproportionating micro-organisms at the time of barite deposition (Roerdink et al, 2013). In addition to a lack of microbial processing of zero-valent sulfur, environmental changes in the hydrothermal system may be responsible for the shifts in sulfur cycling from the pre-3.52 Ga to the 3.52 Ga setting. Since no further barite horizons are known in the underlying rocks at Londozi and hydrothermal activity appears to be exclusively represented by localized silicification of pillow basalts (Section 2.2), the pre-3.52 Ga system was presumably barite-free, reflecting the low sulfate concentrations in the Paleoarchean ocean (possibly less than 2.5 μM, Crowe et al., 2014). In such a system, the atmospheric supply of elemental sulfur was apparently large enough compared to the sulfate-derived sulfide to become incorporated in the pyrite record. In contrast, sulfate levels were probably locally elevated at 3.52 Ga, which led to deposition of the barite (cf. Roerdink et al, 2012), and as a result the elemental sulfur source was temporarily swamped by sulfide derived from oxidized sulfur.

5.3. Constraining sulfur sources of the Londozi pyrite

Our model results (Fig. 4) demonstrate that a mixture of 10% atmospheric sulfur with 90% juvenile sulfur, combined with sulfide derived from reduction of the seawater sulfate pool (barite), produces a 4-component mixing field that is consistent with the observed variation in the pyrite sulfur isotope data as well as the non-zero intercept of the $\Delta^{36}S$-$\Delta^{33}S$ trend. Note that the non-linearity is calculated but not indicated as curved lines in Fig. 4, because effects on final $\Delta^{33}S$ and $\Delta^{36}S$-values are smaller than the analytical precision. Based on our model, we can identify distinct sulfur sources for each individual sample. Isotopic compositions from pyrite in sample LON-10-21a largely plot onto mixing lines (both in $\delta^{34}S$-$\Delta^{33}S$ and $\Delta^{33}S$-$\Delta^{36}S$ space) between the elemental sulfur-derived end member on the deep mixing array (Reservoir 1) and ^{34}S-depleted sulfide derived from reduced seawater sulfate (Reservoir 4), although a slightly larger biological isotope effect than the assumed $^{34}\alpha = 0.985$ is required to explain the few samples plotting above the mixing line in $\delta^{34}S$-$\Delta^{33}S$. In contrast, sulfide from samples LON-10-21b, TR-01 and TR-03 carries a negative $\Delta^{33}S$ and positive $\Delta^{36}S$-signature suggesting a sulfide-component derived from photochemical sulfate (Reservoir 2) in the source region of the hydrothermal fluid. The composition of pyrite in samples LON-10-21b and TR-01 can be explained by mixing of this deep sulfur with sulfide derived from reduced seawater sulfate with variable degrees of isotopic fractionation (Reservoirs 3 and 4), as well as additional input of juvenile sulfur to the seafloor, either from direct hydrothermal degassing or leaching of sulfur from volcanic host rocks without S-MIF. In contrast, barite-hosted pyrite in sample TR-03 lacks this additional magmatic sulfur component and is dominated by mixing lines between the recycled atmospheric sulfate pool and strongly ^{34}S-depleted sulfide (Reservoir 4). Our model is equally permissible with an asymmetrical photochemical array with larger magnitudes of S-MIF in the elemental sulfur (dashed lines in Fig. 4), for example due to changes in volcanic $SO_2{:}H_2S$ degassing fluxes (Halevy et al., 2010). However, the $\Delta^{36}S$-$\Delta^{33}S$ fields defined by our sulfur isotope
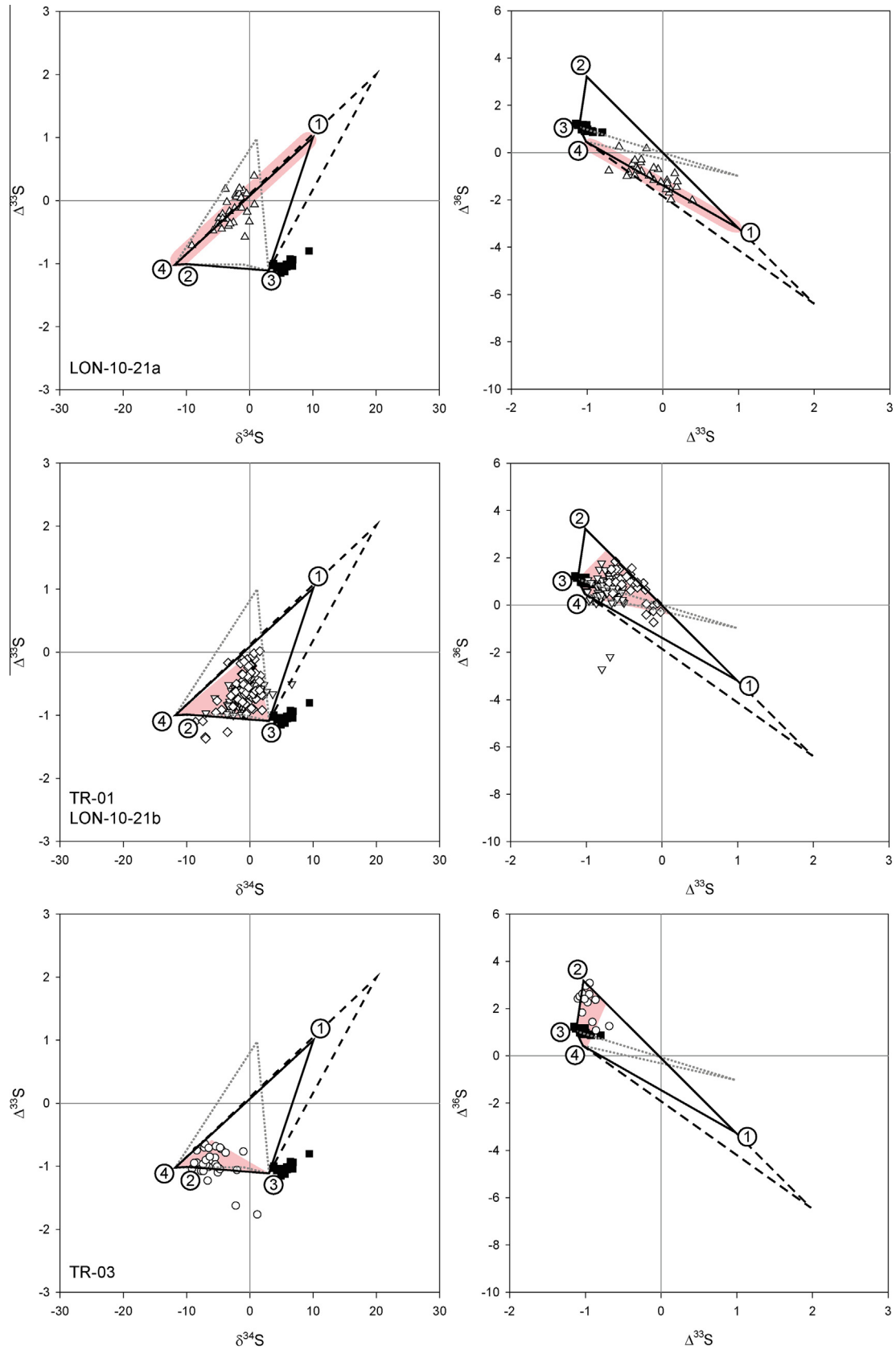
Fig. 4. Modeled mixing fields for the different pyrite samples, with $\Delta^{33}S$–$\delta^{34}S$ plots on the left and $\Delta^{36}S$–$\Delta^{33}S$ plots on the right. Black line: mixing model based on symmetrical photolytic array, dashed line: mixing model based on asymmetrical photolytic array, stippled line: mixing model based on Archean reference array for photolysis. Mixing fields that are consistent with pyrite data in both $\Delta^{33}S$–$\delta^{34}S$ and $\Delta^{36}S$–$\Delta^{33}S$ space are shaded in red. (For interpretation of the references to color in this figure legend, the reader is referred to the web version of this article.)

data (in particular samples LON-10-21a and TR-03) clearly do not match the model results based on the Archean photolytic reference array (stippled grey lines in Fig. 4), confirming the requirement for sulfur produced under different atmospheric conditions than those common in the Archean.

The preserved heterogeneity in pyrite isotopic compositions and sulfur sources further implies that fluid migration pathways varied during the supply of sulfide to the surface environment, so that fluids reacted with the different pools of pre-3.52 Ga photolytic sulfur.

Interaction of fluids with older crustal material in the Londozi hydrothermal system is consistent with the presence of >3.6 Ga crust in the source region of felsic volcanics in the Steynsdorp area, as inferred from radiogenic isotope studies. Exclusively negative $\varepsilon_{Hf(t)}$-values in zircons from a 3530 ± 4 Ma felsic schist sampled *ca.* 2 km north of the Londozi deposit correspond to crustal model ages of 3.8–3.9 Ga (Kröner et al., 2013), whereas slightly negative whole-rock $\varepsilon_{Nd(t)}$-values yield crustal residence ages of 3.6–3.7 Ga (Kröner et al., 1996; Van Kranendonk et al., 2009). In addition, xenocrystic zircons in the 3510 Ma Steynsdorp pluton (Kröner et al., 1996), as well as old (>3600 Ma) zircon grains found in our study (Fig. 1 and SI), verify the importance of an older crustal component in the Londozi region that may have been the source of the pre-3.52 Ga atmospheric sulfur.

5.4. Implications for biosignatures

Minor sulfur isotopic compositions of pyrite minerals associated with Paleoarchean barite deposits have been used as evidence for microbial sulfate reduction as early as 3.5 Ga (Roerdink et al., 2013; Shen et al., 2009; Ueno et al., 2008). Conversely, the interpretation of such biosignatures from the Londozi barite is complicated due to additional non-biological variation in minor sulfur isotope ratios, as described in our hydrothermal mixing model. Most importantly, this partially abiotic origin of the sulfide would have gone unnoticed without our additional *in situ* $\Delta^{36}S$ measurements, since small shifts towards more positive $\Delta^{33}S$-values in the pyrite compared to the barite, as well as the depletion in ^{34}S, would have been consistent with biological reduction of sulfate alone (cf. Shen et al., 2009). Although it remains unknown to what extend this model is relevant for other Paleoarchean barite deposits, on the basis of our study we strongly recommend inclusion of $\Delta^{36}S$ data in future studies on biosignatures in barite-rich Archean hydrothermal systems where abiotic and microbial processes may have operated together.

Finally, our data and model tentatively suggest that atmospheric conditions were sometimes different in the Eoarchean or earliest Paleoarchean compared to most of the Archean eon, perhaps due to different volcanic gas fluxes or less biogenic methane production before 3.52 Ga. Although we do not have evidence that these conditions persisted throughout the entire Eoarchean, this could require the use of a distinct $\Delta^{36}S/\Delta^{33}S$ reference array when using minor sulfur isotope ratios as biosignatures for Eoarchean life. However, more multiple sulfur isotope data is needed from pre-3.52 Ga sulfide samples, preferably obtained by high spatial resolution SIMS analysis, to confirm a different photochemical trend for the earliest era of the Archean.

6. Conclusions

We describe sulfide sources involved in the formation of pyrite associated with the 3.52 Ga Londozi hydrothermal barite deposit in the Barberton Greenstone Belt, Swaziland, based on multiple sulfur isotope data measured *in situ* using secondary ion mass spectrometry. Minor sulfur isotopic compositions argue against a purely bio-

genic or thermochemical origin for the pyrite-sulfur and suggest an additional atmospheric source. However, observation of a significant difference in the $\Delta^{36}S–\Delta^{33}S$ fields defined by the pyrite and ambient Paleoarchean seawater (as recorded in the barite) implies hydrothermal reworking of sulfur that was generated in a chemically distinct pre-3.52 Ga atmosphere. We propose a model that combines a deep mixing array with 10% recycled photolytic and 90% juvenile sulfur, and a surface array representing variable degrees of microbially-reduced ambient seawater sulfate, to explain the variation observed in pyrite $\delta^{34}S$, $\Delta^{33}S$ and $\Delta^{36}S$. Our results indicate that the sulfide S-MIF arrays in this Paleoarchean hydrothermal system do not represent atmospheric conditions at the time of deposition, but reflect reworking of older sulfide. In particular for similar Paleoarchean barite-rich settings where hydrothermal and biological processes may have operated together, deviations in $\Delta^{33}S$ and $\Delta^{36}S$ from the Archean reference array cannot be unambiguously interpreted as evidence for microbial sulfur cycling and the interpretation of biosignatures may be complicated due to overprinting of atmospheric and biological isotopic arrays.

Appendix A. Supplementary data

Supplementary data associated with this article can be found, in the online version, at http://dx.doi.org/10.1016/j.precamres.2016.05.007.

References

Bao, H., Rumble III, D., Lowe, D.R., 2007. The five stable isotope compositions of Fig Tree barites: implications on sulfur cycle in ca. 3.2 Ga oceans. Geochim. Cosmochim. Acta 71, 4868–4879.

Barton, C.M., 1982. Geology and mineral resources of Northwest Swaziland (Barberton Greenstone Belt). Bulletin of the Swaziland Geological Survey and Mines Department 10.

Baublys, K.A., Golding, S.D., Young, E., Kamber, B.S., 2004. Simultaneous determination of 33S V-CDT and 34S V-CDT using masses 48, 49 and 50 on a continuous flow isotope ratio mass spectrometer. Rapid Commun. Mass Spectrom. 18, 2765–2769.

Bekker, A., Barley, M.E., Fiorentini, M.L., Rouxel, O.J., Rumble, D., Beresford, S.W., 2009. Atmospheric sulfur in Archean komatiite-hosted nickel deposits. Science 326, 1086–1089.

Cabral, R.A., Jackson, M.G., Rose-Koga, E.F., Koga, K.T., Whitehouse, M.J., Antonelli, M.A., Farquhar, J., Day, J.M.D., Hauri, E.H., 2013. Anomalous sulphur isotopes in plume lavas reveal deep mantle storage of Archean crust. Nature 496, 490–493.

Claire, M.W., Kasting, J.F., Domagal-Goldman, S.D., Stüeken, E.E., Buick, R., Meadows, V.S., 2014. Modeling the signature of sulfur mass-independent fractionation produced in the Archean atmosphere. Geochim. Cosmochim. Acta 141, 365–380.

Corfu, F., Hanchar, J.M., Hoskin, P.W.O., Kinny, P., 2003. Atlas of zircon textures. In: Hanchar, J.M., Hoskin, P.W.O. (Eds.), Zircon. Reviews in Mineralogy and Geochemistry 53. Mineralogical Society of America.

Crowe, D.E., Vaughan, R.G., 1996. Characterization and use of isotopically homogeneous standards for in situ laser microprobe analysis of 34S/32S ratios. Am. Mineral. 81, 187–193.

Crowe, S.A., Paris, G., Katsev, S., Jones, C., Kim, S.-T., Zerkle, A.L., Nomosatryo, S., Fowle, D.A., Adkins, J.F., Sessions, A.L., Farquhar, J., Canfield, D.E., 2014. Sulfate was a trace constituent of Archean seawater. Science 346, 735–739.

Danielache, S.O., Hattori, S., Johnson, M.S., Ueno, Y., Nanbu, S., Yoshida, N., 2012. Photoabsorption cross-section measurements of 32S, 33S, 34S, and 36S sulfur dioxide for the B1B1-X1A1 absorption band. J. Geophys. Res.: Atmos. 117, D24301.

Domagal-Goldman, S.D., Kasting, J.F., Johnston, D.T., Farquhar, J., 2008. Organic haze, glaciations and multiple sulfur isotopes in the Mid-Archean Era. Earth Planet. Sci. Lett. 269, 29–40.

Farquhar, J., Bao, H., Thiemens, M., 2000. Atmospheric influence of earth's earliest sulfur cycle. Science 289, 756–758.

Farquhar, J., Cliff, J., Zerkle, A.L., Kamyshny, A., Poulton, S.W., Claire, M., Adams, D., Harms, B., 2013. Pathways for Neoarchean pyrite formation constrained by mass-independent sulfur isotopes. Proc. Natl. Acad. Sci. 110, 17638–17643.

Farquhar, J., Johnston, D.T., Wing, B.A., Habicht, K.S., Canfield, D.E., Airieau, S., Thiemens, M.H., 2003. Multiple sulphur isotopic interpretations of biosynthetic pathways: implications for biological signatures in the sulphur isotope record. Geobiology 1, 27–36.

Farquhar, J., Peters, M., Johnston, D.T., Strauss, H., Masterson, A., Wiechert, U., Kaufman, A.J., 2007. Isotopic evidence for Mesoarchaean anoxia and changing atmospheric sulphur chemistry. Nature 449, 706–709.

Farquhar, J., Savarino, J., Airieau, S., Thiemens, M.H., 2001. Observation of wavelength-sensitive mass-independent sulfur isotope effects during SO_2 photolysis: implications for the early atmosphere. J. Geophys. Res. 106, 32829–32839.

Farquhar, J., Wing, B.A., McKeegan, K.D., Harris, J.W., Cartigny, P., Thiemens, M.H., 2002. Mass-independent sulfur of inclusions in diamond and sulfur recycling on early Earth. Science 298, 2369–2372.

Halevy, I., Johnston, D.T., Schrag, D.P., 2010. Explaining the structure of the Archean mass-independent sulfur isotope record. Science 329, 204–207.

Hoskin, P.W.O., Schaltegger, U., 2003. The composition of zircon and igneous and metamorphic petrogenesis. In: Hanchar, J.M., Hoskin, P.W.O. (Eds.), Zircon. Reviews in Mineralogy and Geochemistry 53. Mineralogical Society of America.

Johnston, D.T., 2011. Multiple sulfur isotopes and the evolution of Earth's surface sulfur cycle. Earth Sci. Rev. 106, 161–183.

Johnston, D.T., Farquhar, J., Canfield, D.E., 2007. Sulfur isotope insights into microbial sulfate reduction: when microbes meet models. Geochim. Cosmochim. Acta 71, 3929–3947.

Johnston, D.T., Farquhar, J., Wing, B.A., Kaufman, A.J., Canfield, D.E., Habicht, K.S., 2005. Multiple sulfur isotope fractionations in biological systems: a case study with sulfate reducers and sulfur disproportionators. Am. J. Sci. 305, 645–660.

Kaufman, A.J., Johnston, D.T., Farquhar, J., Masterson, A.L., Lyons, T.W., Bates, S., Anbar, A.D., Arnold, G.L., Garvin, J., Buick, R., 2007. Late Archean biospheric oxygenation and atmospheric evolution. Science 317, 1900–1903.

Kopf, S., Ono, S., 2012. Sulfur mass-independent fractionation in liquid phase chemistry: UV photolysis of phenacylphenylsulfone as a case study. Geochim. Cosmochim. Acta 85, 160–169.

Kröner, A., Elis Hoffmann, J., Xie, H., Wu, F., Münker, C., Hegner, E., Wong, J., Wan, Y., Liu, D., 2013. Generation of early Archaean felsic greenstone volcanic rocks through crustal melting in the Kaapvaal, craton, southern Africa. Earth Planet. Sci. Lett. 381, 188–197.

Kröner, A., Hegner, E., Wendt, J.I., Byerly, G.R., 1996. The oldest part of the Barberton granitoid-greenstone terrain, South Africa: evidence for crust formation between 3.5 and 3.7 Ga. Precambrian Res. 78, 105–124.

Kurzweil, F., Claire, M., Thomazo, C., Peters, M., Hannington, M., Strauss, H., 2013. Atmospheric sulfur rearrangement 2.7 billion years ago: evidence for oxygenic photosynthesis. Earth Planet. Sci. Lett. 366, 17–26.

Lana, C., Kisters, A.F.M., Stevens, G., 2010. Exhumation of Mesoarchean TTG gneisses from the middle crust: insights from the Steynsdorp core complex, Barberton granitoid-greenstone terrain, South Africa. Geol. Soc. Am. Bull. 122, 183–197.

Ludwig, K.R., 2008. User's Manual for Isoplot 3.70. Berkeley Geochronology Center Special Publication, p. 4.

Lyons, J.R., 2007. Mass-independent fractionation of sulfur isotopes by isotope-selective photodissociation of SO_2. Geophys. Res. Lett., 34

Lyons, J.R., 2009. Atmospherically-derived mass-independent sulfur isotope signatures, and incorporation into sediments. Chem. Geol. 267, 164–174.

Mojzsis, S.J., Coath, C.D., Greenwood, J.P., McKeegan, K.D., Harrison, T.M., 2003. Mass-independent isotope effects in Archean (2.5–3.8 Ga) sedimentary sulfides determined by ion microprobe analysis. Geochim. Cosmochim. Acta 67, 1635–1658.

Oduro, H., Harms, B., Sintim, H.O., Kaufman, A.J., Cody, G., Farquhar, J., 2011. Evidence of magnetic isotope effects during thermochemical sulfate reduction. Proc. Natl. Acad. Sci. 108, 17635–17638.

Ohmoto, H., Goldhaber, M.B., 1997. Sulfur and carbon isotopes. In: Barnes, H.L. (Ed.), Geochemistry of Hydrothermal Ore Deposits. John Wiley & Sons, New York.

Ono, S., Eigenbrode, J.L., Pavlov, A.A., Kharecha, P., Rumble Iii, D., Kasting, J.F., Freeman, K.H., 2003. New insights into Archean sulfur cycle from mass-independent sulfur isotope records from the Hamersley Basin, Australia. Earth Planet. Sci. Lett. 213, 15–30.

Ono, S., Shanks Iii, W.C., Rouxel, O.J., Rumble, D., 2007. S-33 constraints on the seawater sulfate contribution in modern seafloor hydrothermal vent sulfides. Geochim. Cosmochim. Acta 71, 1170–1182.

Ono, S., Whitehill, A.R., Lyons, J.R., 2013. Contribution of isotopologue self-shielding to sulfur mass-independent fractionation during sulfur dioxide photolysis. J. Geophys. Res.: Atmos. 118, 2444–2454.

Ono, S., Wing, B., Johnston, D., Farquhar, J., Rumble, D., 2006. Mass-dependent fractionation of quadruple stable sulfur isotope system as a new tracer of sulfur biogeochemical cycles. Geochim. Cosmochim. Acta 70, 2238–2252.

Papineau, D., Mojzsis, S.J., 2006. Mass-independent fractionation of sulfur isotopes in sulfides from the pre-3770 Ma Isua Supracrustal Belt, West Greenland. Geobiology 4, 227–238.

Pavlov, A.A., Kasting, J.F., 2002. Mass-independent fractionation of sulfur isotopes in Archean sediments: strong evidence for an anoxic Archean atmosphere. Astrobiology 2, 27–41.

Pedersen, R.B., Thorseth, I.H., Nygård, T.E., Lilley, M.D., Kelley, D.S., 2010. Hydrothermal activity at the Arctic mid-ocean ridges. In: Rona, P.A., Devey, C. W., Dyment, J., Murton, B.J. (Eds.), Diversity of Hydrothermal Systems on Slow Spreading Ocean Ridges. AGU, Washington, DC, pp. 67–89.

Philippot, P., Van Zuilen, M., Lepot, K., Thomazo, C., Farquhar, J., Van Kranendonk, M. J., 2007. Early Archaean microorganisms preferred elemental sulfur, not sulfate. Science 317, 534–537.

Philippot, P., van Zuilen, M., Rollion-Bard, C., 2012. Variations in atmospheric sulphur chemistry on early Earth linked to volcanic activity. Nat. Geosci. 5, 668–674.

Reed, M.H., Palandri, J., 2006. Sulfide mineral precipitation from hydrothermal fluids. Rev. Mineral. Geochem. 61, 609–631.

Reimer, T.O., 1980. Archean sedimentary baryte deposits of the Swaziland Supergroup (Barberton Mountain Land, South Africa). Precambrian Res. 12, 393–410.

Roerdink, D.L., Mason, P.R., Whitehouse, M.J., Reimer, T., 2013. High-resolution quadruple sulfur isotope analyses of 3.2 Ga pyrite from the Barberton Greenstone Belt in South Africa reveal distinct environmental controls on sulfide isotopic arrays. Geochim. Cosmochim. Acta 117, 203–215.

Roerdink, D.L., Mason, P.R.D., Farquhar, J., Reimer, T., 2012. Multiple sulfur isotopes in Paleoarchean barites identify an important role for microbial sulfate reduction in the early marine environment. Earth Planet. Sci. Lett. 331–332, 177–186.

Rubatto, D., 2002. Zircon trace element geochemistry: partitioning with garnet and the link between U-Pb ages and metamorphism. Chem. Geol. 184, 123–138.

Shanks, W.C., 2001. Stable isotopes in seafloor hydrothermal systems: vent fluids, hydrothermal deposits, hydrothermal alteration, and microbial processes. Rev. Mineral. Geochem. 43, 469–525.

Shen, Y., Farquhar, J., Masterson, A., Kaufman, A.J., Buick, R., 2009. Evaluating the role of microbial sulfate reduction in the early Archean using quadruple isotope systematics. Earth Planet. Sci. Lett. 279, 383–391.

Thomassot, E., O'Neil, J., Francis, D., Cartigny, P., Wing, B.A., 2015. Atmospheric record in the Hadean Eon from multiple sulfur isotope measurements in Nuvvuagittuq Greenstone Belt (Nunavik, Quebec). Proc. Natl. Acad. Sci. 112, 707–712.

Ueno, Y., Ono, S., Rumble, D., Maruyama, S., 2008. Quadruple sulfur isotope analysis of ca. 3.5 Ga Dresser Formation: new evidence for microbial sulfate reduction in the early Archean. Geochim. Cosmochim. Acta 72, 5675–5691.

Van Kranendonk, M.J., Kröner, A., Hegner, E., Connelly, J., 2009. Age, lithology and structural evolution of the c. 3.53 Ga Theespruit Formation in the Tjakastad area, southwestern Barberton Greenstone Belt, South Africa, with implications for Archean tectonics. Chem. Geol. 261, 115–139.

Van Kranendonk, M.J., Pirajno, F., 2004. Geochemistry of metabasalts and hydrothermal alteration zones associated with c. 3.45 Ga chert and barite deposits: implications for the geological setting of the Warrawoona Group, Pilbara Craton, Australia. Geochem.: Explor. Environ., Anal. 4, 253–278.

Wacey, D., Noffke, N., Cliff, J., Barley, M.E., Farquhar, J., 2015. Micro-scale quadruple sulfur isotope analysis of pyrite from the ~3480 Ma Dresser Formation: new insights into sulfur cycling on the early Earth. Precambrian Res. 258, 24–35.

Watanabe, Y., Farquhar, J., Ohmoto, H., 2009. Anomalous fractionations of sulfur isotopes during thermochemical sulfate reduction. Science 324, 370–373.

Whitehill, A.R., Ono, S., 2012. Excitation band dependence of sulfur isotope mass-independent fractionation during photochemistry of sulfur dioxide using broadband light sources. Geochim. Cosmochim. Acta 94, 238–253.

Whitehill, A.R., Xie, C., Hu, X., Xie, D., Guo, H., Ono, S., 2013. Vibronic origin of sulfur mass-independent isotope effect in photoexcitation of SO_2 and the implications to the early earth's atmosphere. Proc. Natl. Acad. Sci. 110, 17697–17702.

Whitehouse, M.J., 2013. Multiple sulfur isotope determination by SIMS: evaluation of reference sulfides for $\Delta^{33}S$ with observations and a case study on the determination of $\Delta^{36}S$. Geostand. Geoanal. Res. 37, 19–33.

Whitehouse, M.J., Kamber, B.S., Fedo, C.M., Lepland, A., 2005. Integrated Pb- and S-isotope investigation of sulphide minerals from the early Archaean of southwest Greenland. Chem. Geol. 222, 112–131.

Williams, I.S., Buick, I.S., Cartwright, I., 1996. An extended episode of early Mesoproterozoic metamorphic fluid flow in the Reynolds Range, central Australia. J. Metamorph. Geol. 14, 29–47.

Zerkle, A.L., Claire, M.W., Domagal-Goldman, S.D., Farquhar, J., Poulton, S.W., 2012. A bistable organic-rich atmosphere on the Neoarchean Earth. Nat. Geosci. 5, 359–363.